Flash upcycling of waste glass fiber-reinforced plastics to phase-controllable silicon carbide

Yi Cheng,[1,†] Jinhang Chen,[1,†] Bing Deng,[1,†] Weiyin Chen,[1] Karla J. Silva,[1] Lucas Eddy,[1,2,3] Gang Wu,[4] Ying Chen,[1] Bowen Li,[1] Carter Kittrell,[1] Shichen Xu,[1] Tengda Si,[1] Angel Martí,[1,5,6] Boris I. Yakobson,[1,3,5] Yufeng Zhao,[5,7,*] and James M. Tour[1,3,5,8,*]

[1] Department of Chemistry, Rice University, Houston, Texas, 77005, USA.

[2] Applied Physics Program, Rice University, Houston, Texas, 77005, USA.

[3] Smalley-Curl Institute, Rice University, Houston, Texas, 77005, USA.

[4] Department of Internal Medicine, University of Texas McGovern Medical School, Houston, Texas, 77030, USA.

[5] Department of Materials Science and NanoEngineering, Rice University, Houston, Texas, 77005, USA.

[6] Department of Bioengineering, Rice University, Houston, Texas, 77005, USA.

[7] Corban University, 5000 Deer Park Drive SE, Salem, Oregon, 97317, USA.

[8] NanoCarbon Center and the Rice Advanced Materials Institute, Rice University, Houston, Texas, 77005, USA.

[†] These authors contributed equally: Yi Cheng, Jinhang Chen, Bing Deng.

* Corresponding authors: J.M.T. (tour@rice.edu), Y.Z. (YZhao@corban.edu).

Abstract

The increasing use of fiber-reinforced plastic has triggered an urgent demand for its recycling once it reaches its end-of-life. Currently, landfilling and incineration are major disposal methods of fiber-reinforced plastic, which lead to undesirable waste of resources and environmental contamination. To address this issue, we disclose a solvent-free and energy-efficient flash upcycling method to convert the mixture of glass fiber-reinforced plastic and carbon fiber-reinforced plastic into SiC powders within seconds and in yields of >90%. By modulating input pulse voltages and flash times, SiC with two different phases, 3C-SiC and 6H-SiC, can be selectively synthesized, each with phase purity of 90-99%. Theoretical simulations reveal that the increasing content of Si vacancy during flash process dominates the phase transformation from 3C-SiC to 6H-SiC. The SiC powders are further used as the anode material for lithium-ion batteries, which yields a phase-dependent performance. The 3C-SiC anode exhibits superior reversible capacity (741 mAh·g^{-1} at 0.2 C) and rate performance over the 6H-SiC anode (626 mAh·g^{-1} at 0.2 C), while both show excellent cycling stability (~95% capacity retention after 200 cycles). Life cycle assessment reveals the flash upcycling process greatly reduces the energy demand, greenhouse gas emission and water consumption over other recycling processes.

Fiber-reinforced plastic (FRP), with the structure of reinforce fibers embedded into a polymer matrix, is a robust composite material[1,2]. Glass fiber-reinforced plastic (GFRP) accounts for 95% of all FRP with merits of light weight, chemical stability, and excellent mechanical properties[3-6], and has been widely used in various platforms ranging from the automotive and aerospace industries to wind turbine blades and sports equipment. It has been estimated that global annual demand for GFRP will exceed 6 million tonnes by 2030, with an annual growth rate of ~10% (ref[7]). However, the life span of the GFRP can only last for 10-40 years[8,9], leading to the disposal of millions of tonnes of GFRP.

Currently, more than half of the waste GFRP is directly landfilled, since it is regarded as the least expensive and simplest disposal route[10,11]. However, most of the thermosetting plastic matrix of GFRP is very slow to degrade by natural decomposition or microbiological treatment[12,13]. The incineration[14,15] and solvolysis method[16,17] enable the reuse of the glass fiber by combusting the polymer matrix or dissolving it using chemical reagents, such as highly concentrated acids or alkalis, and then the glass fiber is remolded. However, the polymer removal process often leads to additional greenhouse gas (GHG) emissions or solvent consumption, resulting in secondary waste streams. Upcycling of GFRP into functional materials, like silicon carbide (SiC), represents a promising value-added route. SiC is a high-performance reinforcement and semiconducting material with high mechanical strength, high-temperature stability, high thermal conductivity and a wide bandgap[18,19]. Conventionally, SiC synthesis methods include chemical vapor deposition (CVD)[20,21], physical vapor transport (PVT)[22,23] and Acheson carbothermic reduction (ACR)[24,25]. The CVD and PVT methods often require a specific temperature gradient and a large supply of carrier gas[20,22], while the ACR process needs annealing for hours or even days at high temperature (>1500 °C) to complete the reaction[24-26], leading to high energy consumption.

Recently, direct electrical heating has emerged as a time- and energy-efficient method for materials synthesis[27,28] and waste management[29,30]. Through the equipment design and process optimization, this electrical heating method has become as an effective way to synthesize high-entropy nanoparticles[31,32] and sinter advanced ceramic[33,34], which can be further applied as the energy-storage materials[35,36] or catalysts[37,38]. Our group developed the flash Joule heating method to convert various carbon resources into turbostratic graphene[39]. It can be further extended to waste management for plastic upcycling[40,41], heavy metal recovery and removal[42,43], and battery materials recycling[44,45]. We hypothesized that the direct electric heating could provide a promising rapid and energy-efficient alternative to achieve GFRP upcycling.

Here, we report a flash carbothermic reduction (FCR) method to upcycle GFRP into SiC. During the FCR process, pre-milled GFRP is mixed with the milled waste carbon fiber-reinforced plastic (CFRP), which is used as the conductive additive. With the electric pulse input, the temperature reaches 1600 – 2900 °C with rapid heating (~10^4 °C s^{-1}) and cooling rates (~10^3 °C s^{-1}). Under such a high temperature, silicon dioxide is carbothermically reduced to SiC within seconds. By modulating the input voltage and the pulse times during the FCR process, we can effectively achieve the phase engineering and selective synthesis of SiC powders, as either the 3C or 6H phase. The as-fabricated SiC is further used as the anode material for lithium-ion batteries (LIBs) and its phase-dependent performance is explored. The 3C-SiC anode exhibits a superior capacity of 741 mAh g^{-1} at 0.2 C after 200 cycles compared with 626 mAh g^{-1} for 6H-SiC, as well as a better rate performance. Benefitting from the rapid reaction process and ultrafast heating and cooling rates, the FCR process is highly cost- and energy-efficient. A life cycle assessment (LCA) revealed that the FCR process reduces energy consumption by 77-97% compared with solvolysis and incineration, while decreasing GHG emission by ~80% compared with incineration. The estimated cost for the synthesis of 3C-SiC is as low as ~\$0.047 per kilogram.

Results

Ultrafast upcycling waste FRP by flash carbothermic reduction

Before the FCR process, the waste GFRP and CFRP were ground and milled into micrometer-sized powders (Step 1, Fig. 1a). The milled GFRP powder consists of 63 wt% amorphous SiO_2 and 37 wt% polymer coating (Supplementary Figs. 1 and 2). The milled CFRP powder, mainly composed of low crystalline and defective carbon, maintains a comparable conductivity with the initial CFRP and is thus suitable to serve as conductive additive for the FCR process (Supplementary Figs. 3 and 4).

In the FCR process, the mixture of the GFRP and CFRP was slightly compressed inside a quartz tube with two graphite electrodes on each side, which were connected to the external capacitor bank (Step 2, Fig. 1a and Supplementary Fig. 5). The CFRP serves as both the conductive additive and the carbothermic reduction agent. During the flash process, the current pulse passed through the sample with a high-voltage input, bringing the sample to a high temperature within milliseconds. Typically, with the GFRP and CFRP mass ratio of 2:1, the sample resistance is ~1.5 Ω (Supplementary Table 1). With the input voltage of 150 V, the maximum current passing through the sample reaches ~350 A within the discharging time of 1 s (Fig. 1b). The sample temperature profile was measured using an infrared thermometer, where the peak temperature was recorded to be ~2900 °C with an ultrafast heating (~10^4 °C s^{-1}) and cooling rate (~10^3 °C s^{-1}) under the input voltage of 150 V (Fig. 1c). At such a high temperature, SiO_2 in GFRP can be carbothermically reduced into SiC and the excess carbon would be converted into flash graphene[39].

To optimize the reaction conditions, we conducted thermodynamic analysis of carbothermic reduction of SiO_2. According to the plot of Gibbs free energy change (ΔG) *vs.* temperature, the increase of carbon/SiO_2 ratio can effectively decrease the reaction temperature from ~2450 °C to ~1600 °C (Fig. 1d). Consequently, the carbon was excessively supplied during FCR process to ensure the complete conversion from SiO_2 to SiC. By modulating the flash input voltage from 80 to 150 V, the flash peak temperature can be tailored in the range of 1600 – 2900 °C, which meets the temperature requirement for SiC synthesis (Supplementary Figs. 6 and 7).

During the FCR process, CO was identified as the main gaseous product with a small quantity of CO_2 and trace amounts of organic compounds, such as acetone, hexane, benzene and toluene, according to the gas chromatography-mass spectra (GC-MS, Supplementary Figs. 8 and 9). With the increase of the input GFRP/CFRP mass ratio, the CO/CO_2 mole ratio in the FCR-evolved gas decreases (Supplementary Fig. 10), which is consistent well with the calculations in Fig. 1d. The input GFRP/CFRP mass ratio is also related to sample conductivities, where certain amounts of CFRP is required to ensure suitable conductivity of the sample for flash reaction. Specifically, the input GFRP/CFRP mass ratio can be modulated from 0.25 to 3, and the obtained SiC contents in the flash products can be tailored from 7.6 wt% to 85 wt% correspondingly (Supplementary Figs. 11 and 12).

Phase-controlled synthesis of SiC

The structure of SiC varies depending on the arrangement of silicon and carbon atoms, which significantly affects its properties and performance in applications[46,47]. For example, 3C-SiC has a smaller bandgap, lower thermal conductivity, higher electron mobility, and higher hardness than 6H-SiC[48,49]. Therefore, it is helpful to control the crystal phases of SiC for optimizing its properties and enabling its wide-range applications. However, the phase control of SiC is challenging, because the SiC phase can be influenced by multiple parameters including reaction precursors, pressure, and temperature[50,51].

The 3C-SiC has a cubic lattice structure with one silicon atom at the center and eight carbon atoms at the corners of each unit cell (left in Fig. 2a). In contrast, the 6H-SiC has a hexagonal structure with carbon atoms located at the hexagonal lattice sites and silicon atoms occupying the interstitial sites between the carbon atoms (right in Fig. 2a)[48,49]. During the FCR process, we discovered that by modulating flash voltages and flash times, phase-controllable 3C-SiC and 6H-SiC can be selectively synthesized. Specifically, phase-pure 3C-SiC was synthesized with an input voltage of 100 V by single flash, according to the X-ray diffraction (XRD) patterns (Supplementary Fig. 13a). Further increasing voltage to 150 V and flashing for 10 times facilitated its phase transformation to 6H-SiC (Supplementary Fig. 13b). Note that the diffraction peak at ~26° is ascribed to the graphene that formed inside the as-synthesized SiC powders[39]. In Raman spectra, in addition to the characteristic D (~1350 cm^{-1}), G (~1580 cm^{-1}) and 2D (~2680 cm^{-1}) bands of flash graphene, the representative TO (~790 cm^{-1}) and LO (~970 cm^{-1}) peaks were observed for both 3C-SiC and 6H-SiC (Supplementary Fig. 14). The additional TA (~505 cm^{-1}) and LA (~240 cm^{-1}) peaks of 6H-SiC are ascribed to its higher symmetric modes than 3C-SiC (ref[52]). To characterize the electronic structure of as-synthesized SiC, X-ray photoelectron spectroscopy (XPS) measurements were conducted (Fig. 2b, Supplementary Figs. 15 and 16). Different from the existence of Si-O (~103 eV) and C-O (~288 eV) peaks for the GFRP precursors (Supplementary Fig. 2c,d), both SiC phases show the distinct Si-C (~100 eV) and C-Si (~282 eV) peaks in the C 1*s* and Si 2*p* core-level spectra (Fig. 2b and Supplementary Fig. 16)[53].

To better compare the intrinsic properties of the two phases of SiC, we calcined the SiC samples at 700 °C in air to remove graphene. After calcination, SiC shows negligible weight loss (<0.5 wt%) in air when heating to 1000 °C, according to the TGA analysis (Supplementary Fig. 17). The XRD patterns of the purified SiC show that phase purity of 3C-SiC and 6H-SiC can reach 99% and 90%, respectively (Fig. 2c). The distinct TO and LO bands in Raman spectra (Fig. 2d), as well as Si-C bond vibration peak (~800 cm^{-1}) in the infrared spectra (Supplementary Fig. 18), confirm the high purity of SiC without any graphene or SiO_2 signals[53], proving that the air calcination is a simple and effective way to purify SiC. Furthermore, diffuse reflectance ultraviolet visible (UV-Vis) spectra demonstrate the different optical properties of these SiC powders, where 3C-SiC has a smaller bandgap (2.45 eV) compared with 6H-SiC (2.86 eV, Fig. 2e and Supplementary Fig. 19). Morphology characterization by scanning electron microscopy (SEM) shows that 3C-SiC and 6H-SiC powders have similar lateral sizes of 2-3 μm (Supplementary Fig. 20). The energy dispersive spectroscopy (EDS) mapping images exhibit uniform distribution of Si and C signals with negligible O signal (Supplementary Figs. 21 and 22). The high-resolution transmission electron microscopy (HRTEM) images further revealed the different atomic arrangement and lattice fringes of the two phases (Fig. 2f,g,i,j). The 0.25 nm interplanar spacing (*d*) corresponds to the (111) plane of 3C-SiC (Fig. 2g), while the *d* at 0.26 nm corresponds to the (010) plane of 6H-SiC (Fig. 2j). The distinct selected-area electron diffraction (SAED) patterns further confirm the structural difference of 3C-SiC and 6H-SiC (Fig. 2h,k). The silicon-based yield was tested by inductively coupled plasma mass spectrometry (ICP-MS), which maintained a high value of 94% and 91% for 3C-SiC and 6H-SiC, respectively, indicating that our FCR process leads to negligible silicon loss (Supplementary Fig. 23).

Mechanism of the phase transformation process

To investigate the SiC phase transformation process, we calculated the phase ratios of SiC samples synthesized under different input voltage and flash times from the XRD patterns (Fig. 3a,b and Supplementary Fig. 24). It is observed that the increase of input voltage and flash times leads to the conversion from 3C-SiC to 6H-SiC, indicating that higher reaction temperature and longer reaction time facilitate the phase transformation.

To explain the phase transformation mechanism, we first characterized the detailed structural feature of these two phases. By using electron paramagnetic resonance (EPR) spectroscopy, Si vacancy was detected in both 3C-SiC and 6H-SiC. The different EPR line shapes of 3C-SiC and 6H-SiC suggest the different environments of Si vacancy[54] (Fig. 3c). The high temperature (~2900 °C, 150 V) during multiple FCR processes can lead to continuous evaporation of silicon atoms, contributing to higher content of silicon vacancy in 6H-SiC (Fig. 3d).

Furthermore, density functional theory (DFT) calculations were employed to depict the energy landscape of the Si-C system (Fig. 3e,f). It is shown that silicon vacancy dominates the formation energy of the Si-C phases, and serves as a key factor for the SiC phase transformation (Fig. 3e,f). With a low content of silicon vacancy (<10 at%), 3C-SiC exhibits a lower formation energy than 6H-SiC, while 6H-SiC is more thermodynamically stable with a higher content of silicon vacancy (>10 at%, Fig. 3e,f). When further considering the possible double-silicon-vacancy in SiC, the trend of the phase-dependent formation energy is similar, where 3C-SiC is more stable with a lower content of silicon vacancy and 6H-SiC is more stable with a higher content of silicon vacancy (Supplementary Figs. 25 and 26). It is worth mentioning that conventional carbothermal reduction processes, involving hours to days of reaction time[24,25], are unfavorable for SiC phase control. In contrast, in our FCR process, the phase controllability benefits from the ultrafast heating and cooling rates, and precise energy input, where the 3C-SiC and 6H-SiC can be selectively synthesized.

LIB performance of SiC-based anode material

SiC with Si–C bilayer stacking structure provides an ideal space for lithium-ion intercalation and is regarded as a potential anode material for LIBs[55,56]. The electrochemical properties of SiC, including carrier density, electron conductivity and ion diffusion performance are highly dependent on its phase[46,49]. Therefore, phase control is important for the performance of SiC anodes in LIBs. We first applied the FCR-synthesized SiC with graphene residue and the bare SiC after calcination as the anodes in coin cells with lithium chips serving as the counter electrodes. It was observed that the inclusion of graphene in the anode improves its performance, with an optimal SiC ratio of ~60 wt% (Supplementary Fig. 27). This improvement of the anode performance can be attributed to the enhanced carrier density and better electrical conductivity of SiC in the presence of graphene, as demonstrated in the simulated density of states (DOS) band (Supplementary Fig. 28) and electrochemical impedance spectra (EIS, Supplementary Fig. 29).

The battery performances of 3C-SiC and 6H-SiC anodes were further compared. The long-term galvanostatic discharge-charge cycling results reveal that both 3C-SiC and 6H-SiC anodes can maintain a stable capacity over 200 cycles with the capacity loss of ~5% (Fig. 4a-c). However, the 3C-SiC anode exhibits an excellent capacity of 741 $mAh \cdot g^{-1}$ after 200 cycles, which is ~16% higher than that of 6H-SiC (626 $mAh \cdot g^{-1}$). The average specific capacity of 3C-SiC anode is 781, 765, 679, 550 and 309 $mAh \cdot g^{-1}$ at the rate of 0.1 C, 0.2 C, 0.4 C, 0.8 C and 1.6 C, respectively, all of which exhibit enhanced performances compared with those of the 6H-SiC anode (Fig. 4d, Supplementary Fig. 30 and Supplementary Table 2). When using the cycling rate of 0.4 C, the 3C-

SiC anode exhibits 82% capacity retention after 200 cycles, which is higher than that of the 6H-SiC anode (71%, Supplementary Fig. 31).

After cycling, the solid electrolyte interphase (SEI) layer covered the surface of SiC anode continuously and uniformly (Supplementary Fig. 32). The phase, structure and crystallinity of SiC were maintained, as confirmed by XRD patterns and XPS spectra (Supplementary Figs. 33 and 34), proving the excellent stability of SiC as the LIB anode material.

We further investigated the mechanism of the phase-dependent LIB performance of SiC. Firstly, the two phases of SiC powders have comparable specific surface areas, as shown by the Brunauer–Emmett–Teller (BET) characterizations (Supplementary Fig. 35). This eliminates the interference of specific area and pore-size distributions on their LIB performance. Further ICP-MS results show the contents of trace metal impurities, specifically Fe, Ni, Co, Mn and Li, in both 3C-SiC and 6H-SiC are well below 50 ppm, thereby avoiding their negative influence on anode performance[44,57] (Supplementary Fig. 36).

Secondly, cyclic voltammetry (CV) was performed to assess the Li^+ diffusion kinetics (Supplementary Fig. 37). For both 3C-SiC and 6H-SiC anodes, the irreversible lithiation peak at ~0.8 V in the first scan relates to the SEI formation, corresponding to the discharging platform in Fig. 4a,b. After the first-cycle scan, with further increasing potential scan rate, all CV curves exhibited similar shapes during the lithiation/delithiation processes, suggesting the reversible Li^+ insertion and extraction, and small polarization (Fig. 4e,f). Generally, Li^+ storage mainly includes two parts: the diffusion-controlled Faradaic reaction process and the surface-induced capacitive process. The contribution of these two processes can be calculated according to the equation of $i = av^b$, where i is the current, v is the scan rate, a and b are adjustable constants[58]. Here, b can be used to describe various reaction kinetics during the ion-storage process, which was calculated from the slope of log(*i*) versus log(*v*) with the value of ~0.5 (Supplementary Fig. 38) for both 3C-SiC and 6H-SiC anodes. It indicates that the Li^+ diffusion process is the dominant process for the SiC anode[59].

Thirdly, EIS spectra reveal that the 3C-SiC anode has a lower charge-transfer resistances (R_{ct} = 139 Ω, corresponding to the semicircle in the high-to-medium frequencies) compared with that of the 6H-SiC anode (R_{ct} = 181 Ω, Fig. 4g), indicating the higher charge-transfer rate of 3C-SiC anode[60]. The slope in the low-frequency region is related to the Li^+ diffusion process. The higher slope of 3C-SiC anode suggests its higher Li^+ diffusion efficiency (Fig. 4g). After 100 and 200 cycles, the EIS curves exhibit lower charge-transfer resistances and lower slope in the low-frequency region, which indicates the improvement of charge-transfer behavior but a decay in Li^+ diffusion efficiency after cycling (Supplementary Fig. 39). Therefore, the EIS results confirm that Li^+ diffusion is the dominant process for the SiC anode, which is consistent with the aforementioned CV results.

Lastly, the diffusion coefficients of SiC anodes were quantitatively measured by the galvanostatic intermittent titration technique (GITT)[44,61]. The detailed experimental and calculation processes of Li^+ diffusion coefficients are shown in Supplementary Note 1 and Supplementary Fig. 40. The 3C-SiC anode shows a higher Li^+ diffusion coefficient than the 6H-SiC anode under different voltages, with an average increase of 31% and 26% in charge and discharge processes, respectively (Fig. 4h, Supplementary Figs. 41 and 42). These findings support the notion that the enhanced performance of 3C-SiC anode results from the improved Li^+ diffusion.

Based on the excellent half-cell performance, the 3C-SiC anode was further applied as the anode in the full-cell battery with the commercial NMC622 ($LiNi_{0.6}Mn_{0.2}Co_{0.2}O_2$) as the cathode. After 200 cycles, the capacity of the full cell can maintain a high value of 2.39 mAh with a capacity retention of 82% (Fig. 4i), where the areal capacity can be calculated as 1.55 mAh cm^{-2}. It indicates that the flash-upcycled SiC anode material holds promise as an anode material for high-performance rechargeable batteries.

Scalability demonstration, life cycle assessment, and techno-economic analysis.

The FCR method demonstrates good scalability. The upcycling of FRPs and the phase control of SiC mainly depend on the flash peak temperature and the flash duration. Therefore, temperature control is a key factor for the scale-up process. Our initial analysis reveals that the increase of flash voltage and capacitance of the FCR system can enhance the productivity per batch (Supplementary Note 2). Subsequently, we developed a second-generation FCR system with a larger capacitance of $C = 0.624$ F (Supplementary Fig. 43a). With an input voltage of 300 V, the sample temperature can ramp to 2000 °C. ~7 g of SiC sample per batch was synthesized within 5 s (Supplementary Fig. 43) with high uniformity (Supplementary Fig. 44). The FCR process can be potentially integrated to a continuous feed system, enabling continuous upcycling of FRPs, as demonstrated by the conceptual design (Supplementary Fig. 45). Moreover, the flash process is undergoing scale-up for graphene synthesis, *en route* to a productivity of tonnes per day by 2024[39,62]. This capability can be readily harnessed for FRP upcycling purposes.

A comparative cradle-to-gate life cycle assessment (LCA) was conducted to compare the environmental impact and energy demand of the FCR upcycling process with other FRP disposal routes, as listed in Supplementary Note 4, and Supplementary Tables 3-7. Three scenarios were considered in this study (Fig. 5a), namely, solvolysis (the polymer matrix of GFRP and CFRP were dissolved by solvent), incineration (GFRP and CFRP were incinerated and the ash was remolded into fiber) and FCR process (GFRP and CFRP were upcycled into SiC powders by FCR process, and 3C-SiC was taken as the example of output products).

Three environmental impacts, energy demand, GHG emission, and water consumption were analyzed. Benefitting from ultrashort reaction time and high energy efficiency, the FCR process exhibits a significant decrease of energy consumption, GHG emissions and water consumption (Fig. 5b). Specifically, the FCR process exhibits a low cumulative energy demand of 2879 MJ tonne^{-1}, which are ~77% and ~96% lower than that of the solvolysis and incineration recycling processes, respectively (Fig. 5c and Supplementary Table 5). This FCR process also demonstrates a cumulative GHG emission of 1709 kg tonne^{-1}, which is comparable with solvolysis process (1669 kg tonne^{-1}), and ~81% lower than the incineration process (Fig. 5d and Supplementary Table 6). Both the FCR process and incineration processes show minimal cumulative water use, whereas solvolysis process require substantial amounts of water (Supplementary Table 7). When synthesizing 1 kilogram of SiC, the cost for FCR is as low as \$0.047 kg^{-1}, which is ~0.2% and ~3.4% of the solvolysis and incineration processes, respectively, to recycle the corresponding amount of waste FRP (Fig. 5e, Supplementary Tables 8 and 9).

Then, we compared the FCR process with the conventional SiC synthesis processes, such as CVD and ACR. Generally, CVD processes require expensive gaseous precursors, and the deposition rate of SiC is ~10 μm h^{-1} with low silicon utilization yield (<0.1%, Supplementary Table 10)[20,21]. More versatile kinds of precursors can be used for SiC synthesis using carbothermic reduction methods. However, traditional ACR process always lasts for hours, leading to significant energy consumption[24,25]. In contrast, the FCR process only lasts for seconds under a higher temperature (2000 – 3000 °C). The FCR reaction time is three to four orders of magnitude lower than other SiC synthesizing processes (Supplementary Fig. 46 and Supplementary Table 10).

These demonstrate the enormous potential of FCR as an economic and eco-friendly process for FRP upcycling and SiC synthesis.

Discussion

We developed a FCR upcycling method to achieve rapid and energy-efficient upcycling of waste FPR into value-added SiC materials in 1 to 10 s. By modulating flash parameters, ≥ 90% phase-purity 3C-SiC and 6H-SiC can be selectively synthesized. When using SiC as the LIB anode material, its phase-dependent performance was discovered, where the 3C-SiC anode exhibits superior capacity and rate performance compared with that of the 6H-SiC anode. With positive attributes of low energy consumption, low GHG emission, solvent- and water-free reaction, and scalability, the FCR method can be extended to upcycle multiple silicon-containing wastes, including glass. In addition, it is expected that the phase-controllable and easily scaled SiC synthesis would offer opportunities in wider-range applications beyond batteries, such as composite reinforcement, semiconductors, photocatalysis and electrocatalysis. This is a harbinger of waste management methods for future generations.

Methods

Materials. The waste GFRP and chopped CFRP were obtained from McMaster and Amazon, respectively. The milling balls (ZrO_2, 99.5 wt%, MTI Corporation) were used to mill the waste FRP to produce powder. 1-Methyl-2-pyrrolidinone (NMP, 99.5 wt%, Millipore-Sigma), polyvinylidene fluoride binder (PVDF, MTI Corporation) and high-conductive acetylene black (ABHC-01, Soltex Corporation) were used to prepare the battery slurry. The electrolyte was 1 M $LiPF_6$ (battery grade, Millipore-Sigma) mixed with ethylene carbonate (EC), diethyl carbonate

(DEC) and dimethyl carbonate (DMC) (volume ratio of 1:1:1). Lithium chips (D = 16 mm, t = 0.6 mm, 99.9 wt%, MTI Corporation) served as the counter electrode in the half cell. NMC622 ($LiNi_{0.6}Mn_{0.2}Co_{0.2}O_2$, 2.0 mAh cm^{-2}, BE-54E, NEI Corporation) was used as the cathode in the full cell.

FCR system and FRP upcycling process. GFRP and CFRP were ground by a hammer grinder (Wenling LINDA machinery Corporation, DF-15) and then further milled by a planetary ball miller (MSE Supplies, PMV1-0.4 L) for 2 h. Afterwards, the mixture of GFRP and CFRP powder was loaded into a quartz tube (~300 mg per batch) with an inner diameter of 8 mm and outer diameter of 12 mm. The sample resistance was controlled to a value of ~1.5 Ω by compressing the electrodes using a home-made device (Supplementary Fig. 5c). Then, the tube was loaded on a home-made reaction jig and connected to the external flash power system. The jig was put into a vacuum desiccator under ~10 mm Hg pressure to avoid the oxidation of the samples. The capacitor bank (60 mF) was charged by a direct current (DC) supply first. The maximal voltage of the bank can reach to 400 V. The relay with programmable delay time with millisecond control was applied to control the discharging time (Supplementary Fig. 5). The flash temperature was recorded by an infrared (IR) thermometer (Micro-Epsilon) in the range of 1000 – 3000 °C with a detection interval of 1 ms. After flashing, the samples rapidly cooled to room temperature.

For the enlarged sample, a mixture of GFRP powder (~6.7 g) and CFRP powder (~3.3 g) was loaded into a quartz tube with ID of 1.6 cm and OD of 2.0 cm (Supplementary Fig. 43b,c). A second-generation FCR reactor was used with the capacity of 0.624 F (Supplementary Fig. 43a). The capacitors were charged to 300 V prior to each flash. Pulse width modulation system (PWM) was implemented in the FCR system using a LabVIEW program with a frequency of 1000 Hz[63].

The duty cycle of the PWM was set as 10% for 1 s, 20% for 0.5 s, and 50% for 5 s before it drops to 0% (Supplementary Fig. 43d-g).

GC-MS test. During the FCR process, the evolved gas vents from the quartz reaction tube through a hollow electrode and was captured into a sealed tube with pressure gauge using our home-designed jig (Supplementary Fig. 8). The system was purged with argon gas, and evacuated to -75 kPa for 5 times before flash. After flash, the evolved gases were injected into the GC-MS using a gas-tight syringe. The GC-MS instrument used here was an Agilent 8890 GC system equipped with an Agilent HP-5ms low-bleed column (30 m, 0.25 mm internal diameter, 0.25 µm film) with helium as the carrier gas for liquid and headspace sampling. A tandem Agilent 5977B mass selective detector was used for liquid and headspace gas analysis.

Characterization. XRD was performed by the Rigaku SmartLab system with filtered Cu Kα radiation (λ = 1.5406 Å). The FT-IR spectra were obtained by a Thermo Scientific Nicolet 6700 attenuated total reflectance Fourier transform infrared (ATR-FTIR) spectrometer (Waltham, MA, USA). Raman spectra were acquired using a Renishaw Raman inVia microscope system with a laser wavelength of 532 nm, laser power of 5 mW and 50 × lens. XPS spectra were taken by the PHI Quantera XPS system under a pressure of 5×10^{-9} Torr. The survey spectra were collected with steps of 0.5 eV and pass energy of 140 eV. Elemental XPS spectra were collected at a step size of 0.1 eV and pass energy of 26 eV. All XPS spectra were calibrated using the C 1*s* peak at 284.8 eV as the reference. TGA was conducted on the Mettler Toledo TGA/DSC 3+ system at a heating rate of 10 °C min^{-1} under 100 mL·min^{-1} air flow. The SEM images and element analysis by EDS were taken on the FEI Quanta 400 ESEM FEG system at a voltage of 20 kV and working distance of 10 mm. The HRTEM images and SAED patterns were obtained on a JEOL 2100 field emission gun transmission electron microscope at 200 kV. The diffraction patterns were calibrated using an Al standard. UV-Vis diffuse reflectance spectra (DRS) were obtained on a SHIMADZU UV-2450 spectrophotometer equipped with a photomultiplier tube in the detecting range of 200-800 nm. Barium sulfate ($BaSO_4$, FUJIFILM Wako) was used to dilute the samples (5 mg SiC:300 mg $BaSO_4$) and as a reference. BET measurements were performed on a Quantachrome Autosorb-iQ3-MP/Kr BET surface analyzer at 77 K, where N_2 was used as the adsorption/desorption gas. X-band EPR spectra were recorded by a Bruker EMX spectrometer (Billerica, MA). The EPR spectra of the SiC powders were obtained at a temperature of 295 K in a capillary tube at a frequency of 9.32 GHz, microwave power of 1 mW, modulation frequency of 100 kHz, modulation amplitude of 1.0 G, and time constant of 0.17 s. The contents of silicon and metal impurities were tested by ICP-MS using a Perkin Elmer Nexion 300 ICP-MS system, with Periodic Table Mix 1 for ICP (10 mg L^{-1}, 10 wt% HNO_3, Millipore Sigma), as the standard. Before the test, 100 mg of the sample was digested by 5 mL solution mixed with HF (48 wt%, 99.99% trace metals basis, MilliporeSigma), HNO_3 (67–70 wt%, TraceMetal^{TM} Grade, Fisher Chemical) and HCl (37 wt%, 99.99% trace metals basis, MilliporeSigma), where the volume ratio of HF, HNO_3 and HCl is 2:1:3. The digestion was conducted at 95 °C for 12 h. The digested solution was filtered by polyether sulfone (PES) membrane (0.22 μm) and then diluted to a range within the calibration curve (1-1000 ppb) using ultrapure water (MilliporeSigma Aldrich, ACS reagent for ultratrace analysis).

Theoretical calculation.

DFT methods[64] were used as they are implemented in the Vienna Ab-initio Simulation Package (VASP)[65]. A plane wave expansion up to 500 eV was employed in combination with an all-electron-like projector augmented wave (PAW) potential[66]. Exchange-correlation was treated within the generalized gradient approximation (GGA) using the functional parameterized by Perdew and Wang[67]. The bulk structures of 3C-SiC and 6H-SiC were first optimized for calibration. To study the energetics of single-Si-vacancy defects, individual Si atom was removed from a hexagonal 4 × 4 × 6 supercell (6-bilayers in Z direction, with 96 Si-C pairs) and the structure was reconstructed by moving a nearby C atom to the Si vacancy[68]. More homogeneously distributed defects can be accommodated in the supercell without collapsing any of the defects. For the Brillouin zone integration, a 3 × 3 × 1 mesh of Monkhorst-Pack type[69] was used for all supercells. In structure optimization using the conjugate-gradient algorithm as implemented in VASP, both the positions of atoms and the unit cells were fully relaxed with the maximum force on each atom smaller than 0.01 eV $Å^{-1}$. For a more thorough search of the lowest-energy defect structure in SiC, the structures were optimized by annealing at 1500 K in a molecular-dynamics (MD) simulation for 10 ps followed by cooling down to 100 K with a rate of 200 K ps^{-1}. Then, the resulting structures were optimized again. The MD simulation was performed using Nose-Hoover thermostat and NVT ensemble.

The formation energy of reconstructed Si vacancy is expressed using following equation (1):

$$f_V = [E_{tot} - e_{SiC}(N_{SiC} - n_V) - e_C n_V]/n_V. \tag{1}$$

Here, E_{tot} is the total energy of SiC supercell with n_V silicon vacancies, e_{SiC} is the energy per Si-C pair in the supercell of the perfect 3C-SiC (or 6H-SiC) crystal bulk which has N_{SiC} of 96 Si-C pairs, and e_C is the energy per C atom in graphene.

The DOS of bare 3C-SiC and 6H-SiC were calculated based on the optimized crystal structures in primitive cells. The DOS of graphene-coated 3C-SiC and 6H-SiC were computed in 5 × 5 supercell of graphene matching the 4 × 4 surface lattice of SiC.

The calculations of the Gibbs free energy change and vapor pressure under different temperature were conducted by the HSC Chemistry 10 software.

Data availability

All data needed to support the conclusions in the paper are present in the manuscript and/or Supplementary Information. Additional data related to this paper are available upon reasonable request from the corresponding authors.

Acknowledgements

The funding of the research is provided by Air Force Office of Scientific Research (FA9550-22-1-0526) and the U.S. Army Corps of Engineers, ERDC grant (W912HZ-21-2-0050). The authors acknowledge the use of the Electron Microscopy Center (EMC) at Rice University. The characterization equipment used in this project is partly from the Shared Equipment Authority (SEA) at Rice University. The authors thank Dr. Bo Chen of Rice University for helpful discussion of the XPS results.

Author contributions

J.M.T. and Y.C. conceived the idea and designed the experiments. Y.C. conducted the synthesis, and most of the characterizations with the help of J.C., B.D., W.C., B.L., S.X. and T.S. Y.C. and J.C. conducted the assembly and electrochemical tests of the LIBs. B.D. conducted the TEM and

SAED tests. K.J.S. helped with the GC-MS tests. L.E. maintained the flash system and assisted with the scale-up experiments. G.W. conducted the EPR test. Y.C. and A.M. conducted the UV-Vis measurement. C.K. provided the waste GFRP samples. Y.Z. and B.I.Y. conducted the MD and DFT simulation. Y.C. analyzed the simulation results with the assistance of Y.Z. Y.C., J.C., B.D., Y.Z., and J.M.T. wrote and edited the manuscript. All aspects of the research were overseen by J.M.T. All authors discussed the results and commented on the manuscript.

Competing interests

A patent application was filed by Rice University, where Y.C., J.C., B.D., and J.M.T. are listed as the inventors, which has not yet been licensed. The authors declare no other competing interests.

References

1. Goncalves, R. M., Martinho, A. & Oliveira, J. P. Recycling of reinforced glass fibers waste: Current status. *Materials* **15**, 1596 (2022).
2. Cunliffe, A. M. & Williams, P. T. Characterisation of products from the recycling of glass fibre reinforced polyester waste by pyrolysis. *Fuel* **82**, 2223-2230 (2003).
3. Cui, G. et al. Massive growth of graphene quartz fiber as a multifunctional electrode. *ACS Nano* **14**, 5938-5945 (2020).
4. Cheng, Y. et al. Graphene infrared radiation management targeting photothermal conversion for electric-energy-free crude oil collection. *J. Am. Chem. Soc.* **144**, 15562-15568 (2022).
5. Sena-Cruz, J. et al. The effect of surface treatment and environmental actions on the adhesive connection between GFRP laminate surface and fresh FRC. *Constr. Build. Mater.* **258**, 119594 (2020).

6. Sathishkumar, T., Satheeshkumar, S. & Naveen, J. Glass fiber-reinforced polymer composites–a review. *J. Reinf. Plast. Compos.* **33**, 1258-1275 (2014).
7. Xue, X., Liu, S.-Y., Zhang, Z.-Y., Wang, Q.-Z. & Xiao, C.-Z. A technology review of recycling methods for fiber-reinforced thermosets. *J. Reinf. Plast. Compos.* **41**, 459-480 (2021).
8. Karuppannan Gopalraj, S. & Kärki, T. A review on the recycling of waste carbon fibre/glass fibre-reinforced composites: Fibre recovery, properties and life-cycle analysis. *SN Appl. Sci.* **2**, 433 (2020).
9. Jensen, J. P. & Skelton, K. Wind turbine blade recycling: Experiences, challenges and possibilities in a circular economy. *Renew. Sust. Energ. Rev.* **97**, 165-176 (2018).
10. Krauklis, A. E., Karl, C. W., Gagani, A. I. & Jørgensen, J. K. Composite material recycling technology—state-of-the-art and sustainable development for the 2020s. *J. Compos. Sci.* **5**, 28 (2021).
11. Thomason, J., Jenkins, P. & Yang, L. Glass fibre strength—a review with relation to composite recycling. *Fibers* **4**, 18 (2016).
12. Zheng, Y., Yanful, E. K. & Bassi, A. S. A review of plastic waste biodegradation. *Crit. Rev. Biotechnol.* **25**, 243-250 (2005).
13. Bahl, S., Dolma, J., Jyot Singh, J. & Sehgal, S. Biodegradation of plastics: A state of the art review. *Mater. Today: Proc.* **39**, 31-34 (2021).
14. Jacob, A. Composites can be recycled. *Reinf. Plast.* **55**, 45-46 (2011).
15. Naqvi, S. R. et al. A critical review on recycling of end-of-life carbon fibre/glass fibre reinforced composites waste using pyrolysis towards a circular economy. *Resour. Conserv. Recycl.* **136**, 118-129 (2018).

16. Yuyan, L., Linghui, M., Yudong, H. & Lixun, L. Method of recovering the fibrous fraction of glass/epoxy composites. *J. Reinf. Plast. Compos.* **25**, 1525-1533 (2006).
17. Ahrens, A. et al. Catalytic disconnection of C–O bonds in epoxy resins and composites. *Nature* **617**, 730-737 (2023).
18. Wang, J.-F. et al. Magnetic detection under high pressures using designed silicon vacancy centres in silicon carbide. *Nat. Mater.* **22**, 489-494 (2023).
19. Yajima, S., Hayashi, J., Omori, M. & Okamura, K. Development of a silicon carbide fibre with high tensile strength. *Nature* **261**, 683-685 (1976).
20. Booker, I. D., Farkas, I., Ivanov, I. G., Ul Hassan, J. & Janzén, E. Chloride-based SiC growth on a-axis 4H–SiC substrates. *Physica B Condens. Matter* **480**, 23-25 (2016).
21. Clavaguera-Mora, M. T. et al. Growth of SiC films obtained by LPCVD. *Diam. Relat. Mater.* **6**, 1306-1310 (1997).
22. Yan, J. Y., Chen, Q. S., Jiang, Y. N. & Zhang, H. Improvement of the thermal design in the SiC PVT growth process. *J. Cryst. Growth* **385**, 34-37 (2014).
23. Herro, Z. et al. Investigation of mass transport during PVT growth of SiC by ^{13}C labeling of source material. *J. Cryst. Growth* **258**, 261-267 (2003).
24. Shin, Y., Wang, C. M. & Exarhos, G. Synthesis of SiC ceramics by the carbothermal reduction of mineralized wood with silica. *Adv. Mater.* **17**, 73-77 (2005).
25. Guo, X., Zhu, L., Li, W. & Yang, H. Preparation of SiC powders by carbothermal reduction with bamboo charcoal as renewable carbon source. *J. Adv. Ceram.* **2**, 128-134 (2013).
26. Han, Y. C. et al. A general method for rapid synthesis of refractory carbides by low-pressure carbothermal shock reduction. *Proc. Natl Acad. Sci. USA* **119**, e2121848119 (2022).
27. Jiang, R. et al. Ultrafast synthesis for functional nanomaterials. *Cell Rep. Phys. Sci.* **2** (2021).

28. Cheng, Y. et al. Electric current aligning component units during graphene fiber Joule heating. *Adv. Funct. Mater.* **32**, 202103493 (2021).

29. Wyss, K. M., Deng, B. & Tour, J. M. Upcycling and urban mining for nanomaterial synthesis. *Nano Today* **49**, 101781 (2023).

30. Jia, C. et al. Graphene environmental footprint greatly reduced when derived from biomass waste via flash Joule heating. *One Earth* **5**, 1394-1403 (2022).

31. Yao, Y. G. et al. Carbothermal shock synthesis of high-entropy-alloy nanoparticles. *Science* **359**, 1489-1494 (2018).

32. Chen, Y. et al. Ultra-fast self-assembly and stabilization of reactive nanoparticles in reduced graphene oxide films. *Nat. Commun.* **7**, 12332 (2016).

33. Wang, C. et al. A general method to synthesize and sinter bulk ceramics in seconds. *Science* **368**, 521-526 (2020).

34. Deng, B. et al. High-surface-area corundum nanoparticles by resistive hotspot-induced phase transformation. *Nat. Commun.* **13**, 5027 (2022).

35. Zhu, W. et al. Ultrafast non-equilibrium synthesis of cathode materials for Li-ion batteries. *Adv. Mater.* **35**, 2208974 (2023).

36. Jiang, H. et al. Boosting cycling stability by regulating surface oxygen vacancies of LNMO by rapid calcination. *Nano Res.* (2023). https://doi.org/10.1007/s12274-023-6076-1

37. Yu, F. et al. Rapid self-heating synthesis of Fe-based nanomaterial catalyst for advanced oxidation. *Nat. Commun.* **14**, 4975 (2023).

38. Liu, S. et al. Extreme environmental thermal shock induced dislocation-rich Pt nanoparticles boosting hydrogen evolution reaction. *Adv. Mater.* **34**, 2106973-2106979 (2022).

39. Luong, D. X. et al. Gram-scale bottom-up flash graphene synthesis. *Nature* **577**, 647-651 (2020).

40. Dong, Q. et al. Depolymerization of plastics by means of electrified spatiotemporal heating. *Nature* **616**, 488-494 (2023).

41. Wyss, K. M. et al. Upcycling of waste plastic into hybrid carbon nanomaterials. *Adv. Mater.* **35**, 2209621 (2023).

42. Deng, B. et al. Urban mining by flash Joule heating. *Nat. Commun.* **12**, 5794 (2021).

43. Deng, B. et al. Heavy metal removal from coal fly ash for low carbon footprint cement. *Commun. Eng.* **2**, 13 (2023).

44. Chen, W. et al. Flash recycling of graphite anodes. *Adv. Mater.* **35**, e2207303 (2023).

45. Luo, J. et al. Recycle spent graphite to defect-engineered, high-power graphite anode. *Nano Res.* **16**, 4240-4245 (2023).

46. Shen, Z. et al. Tunable fabrication and photoluminescence property of SiC nanowires with different microstructures. *Appl. Surf. Sci.* **506**, 144979 (2020).

47. Huang, J., Zeng, X., Li, H., Xiong, X. & Fu, Y. Influence of the preparation temperature on the phase, microstructure and anti-oxidation property of a SiC coating for C/C composites. *Carbon* **42**, 1517-1521 (2004).

48. Persson, C. & Lindefelt, U. Dependence of energy gaps and effective masses on atomic positions in hexagonal SiC. *J. Appl. Phys.* **86**, 5036-5039 (1999).

49. Kong, L. et al. Two novel SiC phases: Structure, mechanical, and transport properties. *Mater. Res. Express* **7**, 085902 (2020).

50. Shimojo, F. et al. Molecular dynamics simulation of structural transformation in silicon carbide under pressure. *Phys. Rev. Lett.* **84**, 3338 (2000).

51. Yoo, W. S. Y. W. S. & Matsunami, H. M. H. Solid-state phase transformation in cubic silicon carbide. *Jpn. J. Appl. Phys.* **30**, 545 (1991).
52. Feldman, D. W., Parker, J. H., Choyke, W. J. & Patrick, L. Phonon dispersion curves by Raman scattering in SiC, polytypes 3C, 4H, 6H, 15R, and 21R. *Phys. Rev.* **173**, 787-793 (1968).
53. Yu, M., Temeche, E., Indris, S. & Laine, R. M. Adjusting SiO_2 : C mole ratios in rice hull ash (RHA) to control carbothermal reduction to nanostructured SiC, Si_3N_4 or Si_2N_2O composites. *Green Chem.* **23**, 7751-7762 (2021).
54. Son, N. T., Carlsson, P., ul Hassan, J., Magnusson, B. & Janzén, E. Defects and carrier compensation in semi-insulating 4H-SiC substrates. *Phys. Rev. B* **75**, 155204 (2007).
55. Sun, C. et al. Interfacial coupled design of epitaxial graphene@SiC schottky junction with built-in electric field for high-performance anodes of lithium ion batteries. *Nano Energy* **77**, 105092 (2020).
56. Yu, M., Temeche, E., Indris, S., Lai, W. & Laine, R. M. Silicon carbide (SiC) derived from agricultural waste potentially competitive with silicon anodes. *Green Chem.* **24**, 4061-4070 (2022).
57. Li, H. et al. Re-utilization of waste graphite anode materials from spent lithium-ion batteries. *J. Electroanal. Chem.* **932**, 117247 (2023).
58. Qian, J. et al. Boosting fast sodium storage of a large-scalable carbon anode with an ultralong cycle life. *Adv. Energy Mater.* **8**, 1703159 (2018).
59. Chen, C. et al. Na^+ intercalation pseudocapacitance in graphene-coupled titanium oxide enabling ultra-fast sodium storage and long-term cycling. *Nat. Commun.* **6**, 6929 (2015).

60. Kim, N., Park, H., Yoon, N. & Lee, J. K. Zeolite-templated mesoporous silicon particles for advanced lithium-ion battery anodes. *ACS Nano* **12**, 3853-3864 (2018).

61. Yang, X. et al. Amorphous tin-based composite oxide: A high-rate and ultralong-life sodium-ion-storage material. *Adv. Energy Mater.* **8**, 1701827 (2018).

62. Universal matter. Ltd (https://www.universalmatter.com/) is commercially scaling up the FJH process, accessed July 20th, 2023.

63. Eddy, L. et al. Laboratory kilogram-scale graphene production from coal. Preprint at https://doi.org/10.26434/chemrxiv-2023-7z1s2 (2023).

64. Dudarev, S. L., Botton, G. A., Savrasov, S. Y., Humphreys, C. & Sutton, A. P. Electron-energy-loss spectra and the structural stability of nickel oxide: An LSDA+ U study. *Phys. Rev. B* **57**, 1505 (1998).

65. Kresse, G. & Furthmuller, J. Efficient iterative schemes for ab initio total-energy calculations using a plane-wave basis set. *Phys. Rev. B* **54**, 11169-11186 (1996).

66. Blöchl, P. E. Projector augmented-wave method. *Phys. Rev. B* **50**, 17953 (1994).

67. Perdew, J. P. & Wang, Y. Accurate and simple analytic representation of the electron-gas correlation energy. *Phys. Rev. B* **45**, 13244 (1992).

68. Rauls, E., Frauenheim, T., Gali, A. & Deák, P. Theoretical study of vacancy diffusion and vacancy-assisted clustering of antisites in sic. *Phys. Rev. B* **68**, 155208 (2003).

69. Monkhorst, H. J. & Pack, J. D. Special points for brillouin-zone integrations. *Phys. Rev. B* **13**, 5188 (1976).

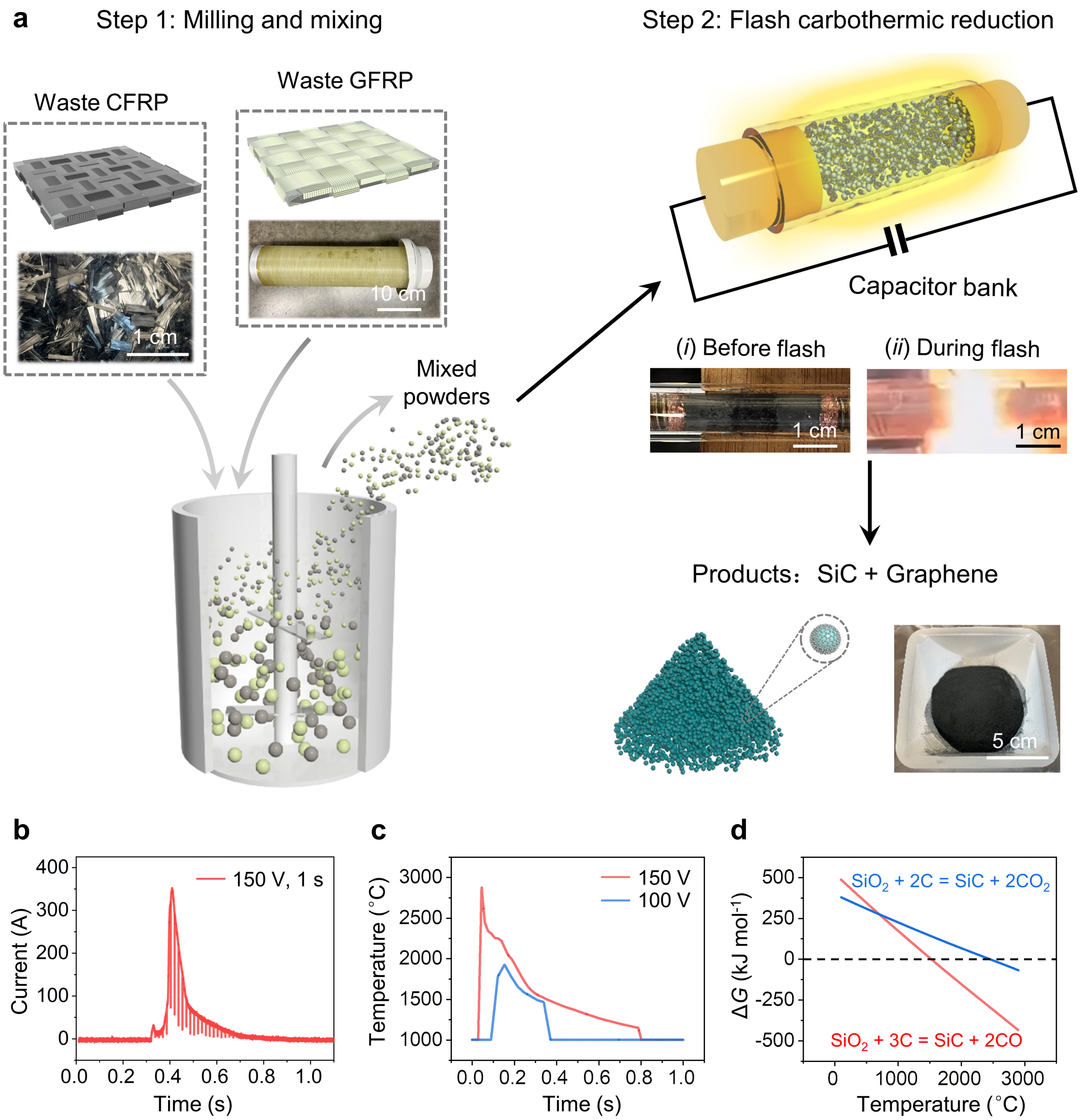

Fig. 1 | Upcycling FRP to silicon carbide by flash carbothermic reduction. a, Schematic of the FCR process for FRP upcycling. Insets in step 1, pictures of waste GFRP disassembled from a Dewar bottle and chopped CFRP. Insets in step 2, pictures of the sample in the quartz tube before (*i*) and during (*ii*) the FCR reaction. **b,** Current curve with an input voltage of 150 V and duration of 1 s during the FCR process. **c,** Real-time temperature curve with the input voltage of 100 V (blue) and 150 V (red) recorded by an infrared thermometer. The temperature detection range of the thermometer is 1000 to 3000 °C. **d,** The relationship between the Gibbs free energy change (ΔG) and temperature with different ratios between SiO_2 and carbon. The horizontal dashed line denotes the ΔG at zero.

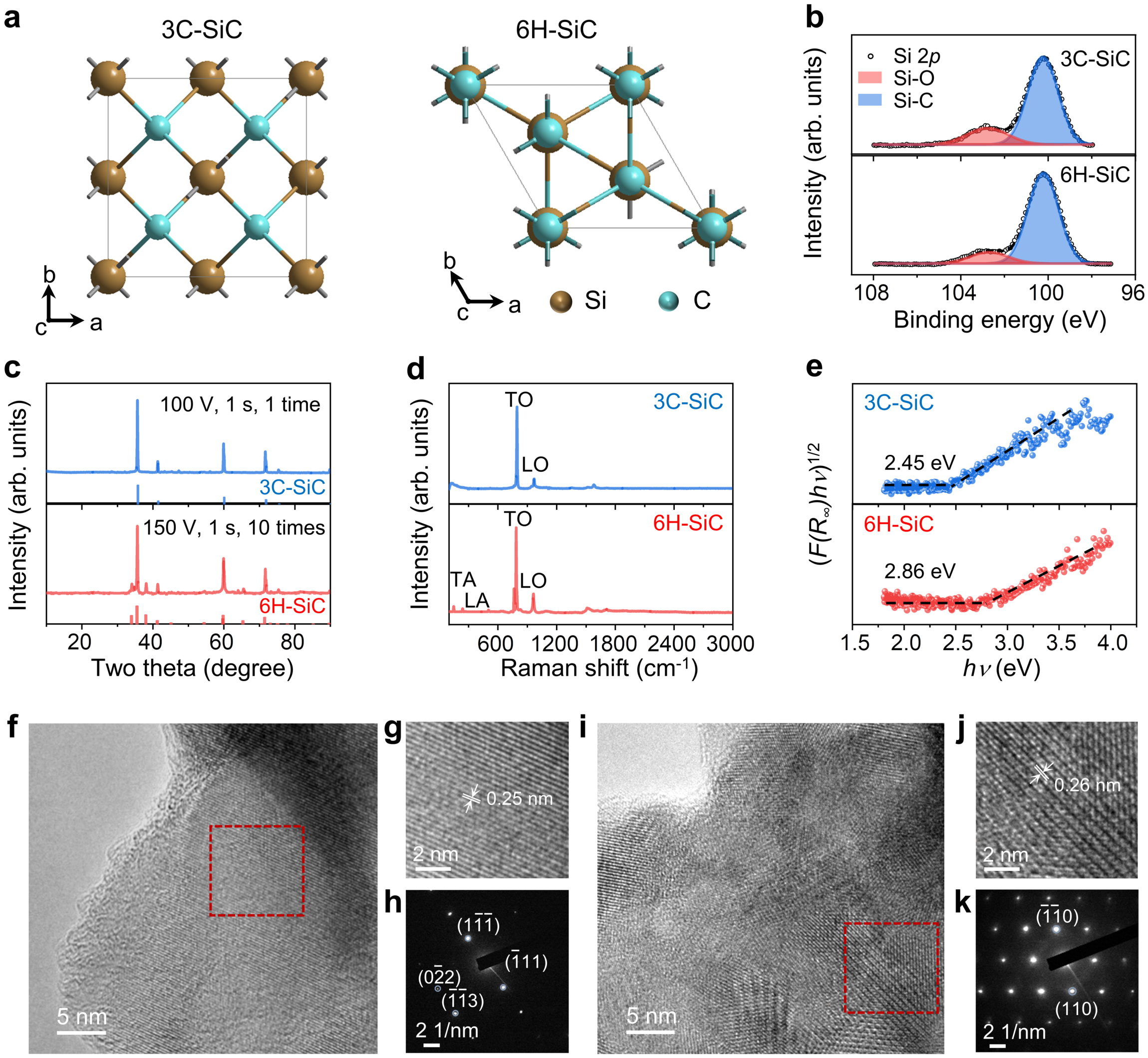

Fig. 2 | Phase controllable synthesis of SiC. a, Crystal structures of 3C-SiC (left) and 6H-SiC (right). **b,** Si 2*p* core-level XPS spectra of 3C-SiC (top) and 6H-SiC (bottom). The small peak of Si-O (~103 eV) may be ascribed to the slight oxidation when exposed to air. **c,** XRD patterns of purified 3C-SiC synthesized at a voltage of 100 V and single flash (top) and purified 6H-SiC synthesized at a voltage of 150 V and 10 flashes (bottom). The PDF reference cards for each are 3C-SiC, 01-073-1708 (blue line); 6H-SiC, 01-075-8314 (red line). **d,** Representative Raman spectra of purified 3C-SiC (top) and 6H-SiC (bottom). TO is the transverse optical mode. LO is the longitudinal optical mode. TA is the transverse acoustic mode. LA is the longitudinal acoustic mode. **e,** Tauc plots of 3C-SiC (top) and 6H-SiC (bottom). **f,** HRTEM image of 3C-SiC. **g,** Zoom-in HRTEM image of 3C-SiC. **h,** SAED pattern of 3C-SiC. **i,** HRTEM image 6H-SiC. **j,** Zoom-in HRTEM image of 6H-SiC. **k,** SAED pattern of 6H-SiC.

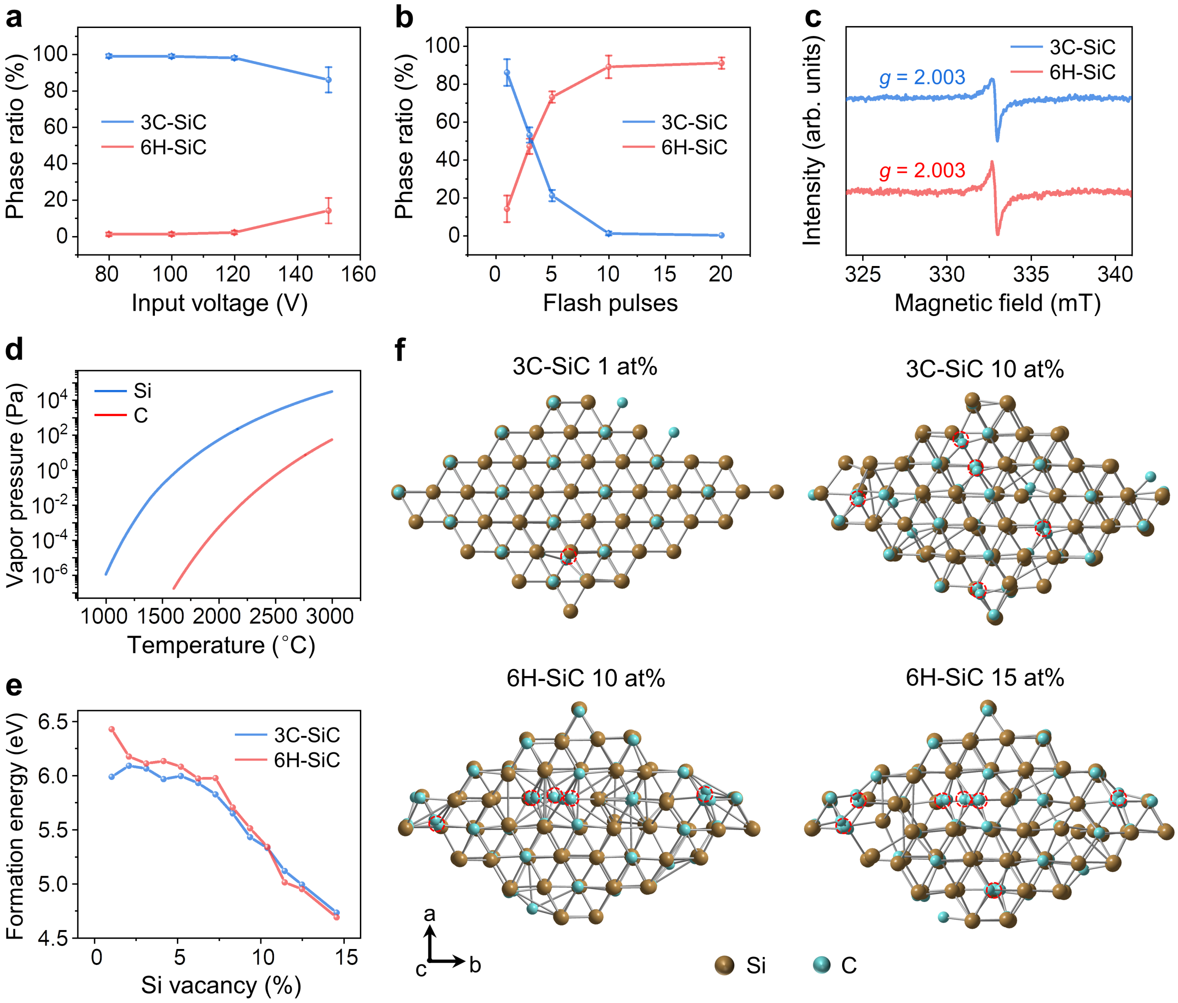

Fig. 3 | Mechanism of SiC phase transformation. a, SiC phase mass ratios versus the input voltage under the one flash pulse. **b,** SiC phase mass ratios versus the flash pulses under the input voltage of 150 V. All error bars in **a,b** represent the standard deviation, where $N = 3$. **c,** EPR spectra of 3C-SiC and 6H-SiC. **d,** Temperature-vapor pressure relationships for silicon and carbon. **e,** Formation energy of 3C-SiC and 6H-SiC with different content of silicon vacancy. **f,** Calculated crystal structures of 3C-SiC (top) and 6H-SiC (bottom) with different atomic content of Si vacancy. The dashed circles denote the silicon vacancies.

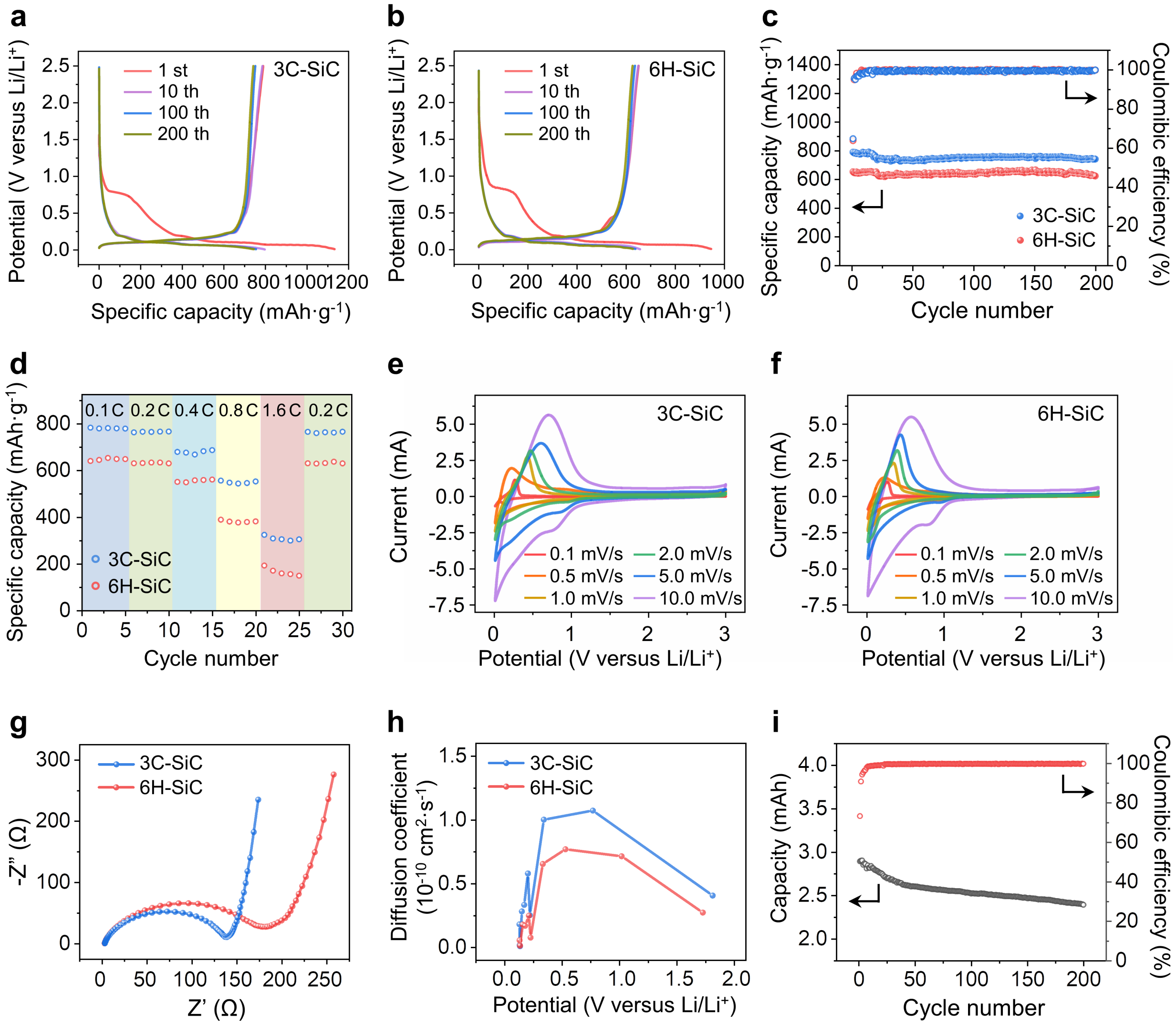

Fig. 4 | Phase dependent LIB performance of SiC anode. **a,** Charge-discharge profiles of 3C-SiC anode at different cycles. **b,** Charge-discharge profiles of 6H-SiC anode at different cycles. **c,** Cycling stability of 3C-SiC anode (blue spot) and 6H-SiC anode (red spot) at 0.2 C. **d,** Rate capacity of 3C-SiC anode (blue spot) and 6H-SiC anode (red spot). **e,** CV curves of 3C-SiC anode at different scan rates. **f,** CV curves of 6H-SiC anode at different scan rates. **g,** Nyquist plots of 3C-SiC anode (blue line) and 6H-SiC anode (red line) before cycling. **h,** The Li$^+$ diffusion coefficient of 3C-SiC anode (blue line) and 6H-SiC anode (red line) during the charging process. **i,** Cycling stability of the full-cell LIB with 3C-SiC anode and NMC622 cathode at 0.2 C.

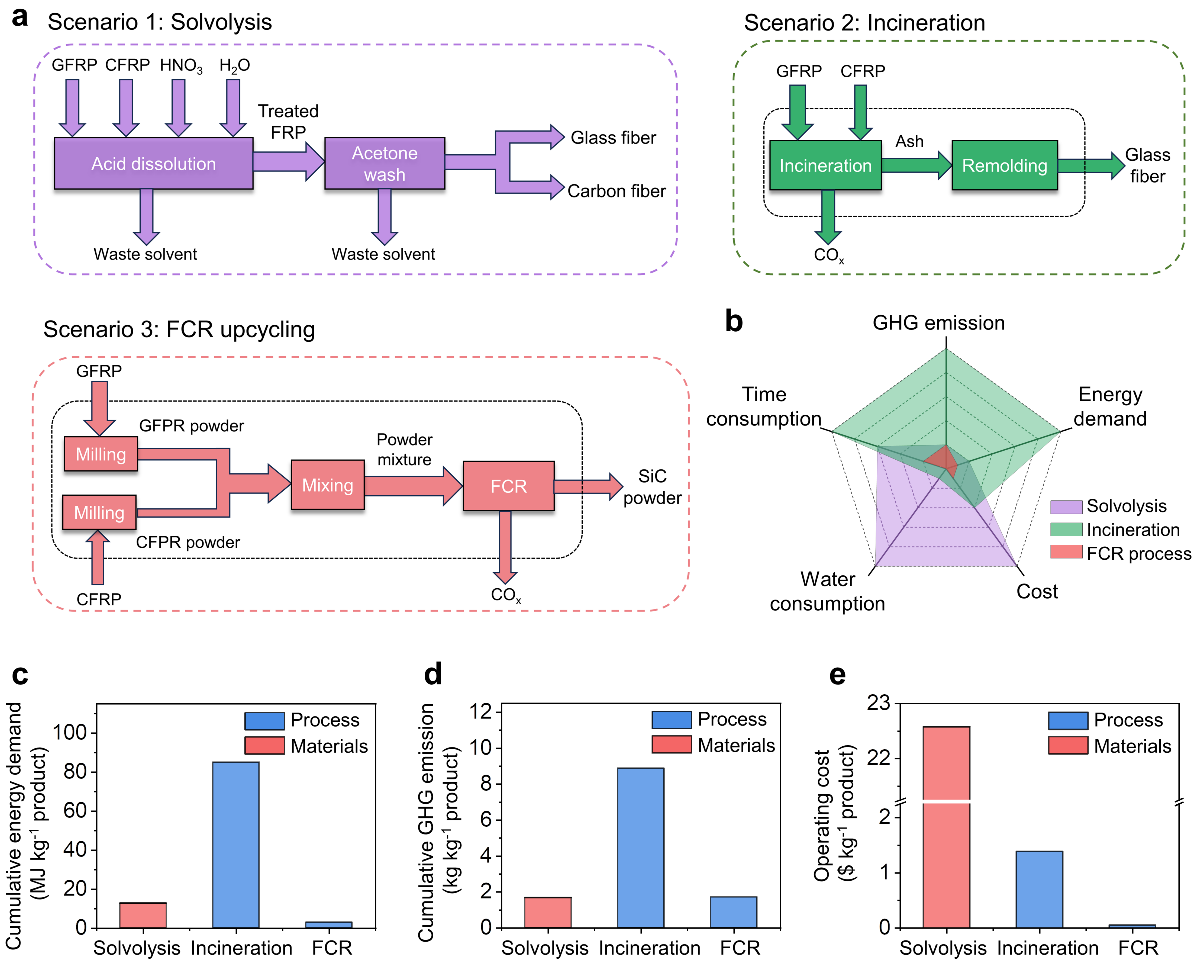

Fig. 5 | LCA for the FRP recycling. a, Materials flow analysis of the solvolysis, incineration and FCR process. **b,** Comprehensive comparisons of the solvolysis, incineration and FCR process. **c,** Comparison of cumulative energy demand. **d,** Comparison of cumulative GHG emission. **e,** Techno-economic comparison. The materials mass flow is normalized to the consumption amounts of GFRP (1.5 tonnes) and CFRP (0.75 tonne) for the production of 1 tonne of SiC during FCR process.